Numerical Investigation of Air Injection in the Endwall Region of a Highly-Loaded Compressor Tandem Stator Configuration

Gladys Gutiérrez Lupinta, Samuele Giannini, Volker Gümmer
Technical University of Munich
School of Engineering and Design
Institute of Turbomachinery and Flight Propulsion
Boltzmannstrasse 15, 85748 Garching
gladys.gutierrez@tum.de

ABSTRACT

The current research focuses on the implementation of air injection in a highly-loaded axial compressor to energize low-momentum flow regions and enhance aerodynamic performance. This study introduces air injection at the casing endwall of a tandem stator in a low-speed compressor, marking the first of its kind for tandem stator configurations. The methodology comprises two phases: an initial numerical investigation of the smooth casing case via steady-state modeling, followed by a parametric study to optimize injection slot geometry and identify beneficial locations. The study quantifies the effects of continuous injection on performance improvement across both design and off-design conditions, with an integrated analysis of aerodynamic losses associated with air injection. The aim is to find optimum arrangements that maximize the advantages of tandem stator vanes, ultimately leading to improved compressor performance.

Keywords: active flow control; injection slots; tandem vanes; axial compressor, CFD, aerodynamics

NOMENCLATURE

Acronyms

GCI	Grid Convergence Index
SC	Smooth Casing
TS	Tandem Stator
DP	Design Point

Greek Letters

α	Inclination Angle
β	Jet Angle
Δ	Increment
η	Polytropic Efficiency
Π	Pressure Ratio
ω	Pressure loss coefficient
ζ	Normalized Chordwise Location

Latin Letters

C_p	Static Pressure Rise Coefficient
CoV	Coefficient of variance
DF	Diffussion Factor
H	Normalized span
Ma	Mach Number
$\dot{m}$	Mass Flow Rate
p	Pressure
Ref	Refined Configurations
R_c	Radius of Curvature
u	Absolute Velocity
w	Width
x	Radial direction
y	Circumferential direction
z	Axial direction

Sub- and Superscripts

inj	Injection
inlet	Injector inlet
inter	Interface Casing - Injector
is	Isentropic
pol	Polytropic
tt	Total to Total
$\overline{x}$	Mass Flow Average of x

INTRODUCTION

To address the evolving demands of environmentally friendly aviation, it is necessary to maximize engine performance while reducing overall weight, length, fuel consumption, and pollutant emissions. The compressor, a critical component, often experiences flow separations in its gaspath, especially near the endwall regions of rotor and stator rows. Therefore, efficient optimization and flow control methods are essential technologies for enhancing compressor performance in future aircraft engines.

Among the various flow control methods explored, air injection stands out as a particularly effective strategy that has undergone extensive research. Works such as [1] have validated its role in enhancing transonic axial compressor aerodynamics through a detailed study on stator air injection. This involved analyzing injector characteristics such as curvature, location, and mass flow rate, which led to improvements in pressure ratio, adiabatic efficiency, stall margin, and stable range, outperforming smooth casing designs. Subsequent studies, including optimization with stator shroud air injection, achieved further aerodynamic enhancements [2]. Additionally, the introduction of discrete holes on the endwall significantly reduced corner separation and loss coefficient in a highly loaded compressor cascade [3].

Advancing this approach, pulsed endwall air injection has demonstrated significant suppression of corner separation, achieving notable reductions in both overall and endwall loss coefficients with lower injection mass flow rates, thus enhancing aerodynamic performance in compressor cascades [4].

Meanwhile, tandem airfoils, employed for their ability to enable higher aerodynamic loading and reduce axial length, exhibit considerable potential for enhancing compressor performance by facilitating rotor designs with increased work coefficients and revealing benefits in pressure rise compared to traditional single aerofoil configurations [5, 6, 7]. However, the integration of tandem stators introduces significant challenges, particularly at the endwalls, where complex flow phenomena can undermine these benefits [8]. To address these challenges, various flow control techniques have been applied to tandem stator vanes. For instance, near-endwall modifications have shown a reduction in corner separation by eliminating low momentum gap-flow [9]. In another study [10], an endwall boundary layer suction compound flow control implemented in a tandem stator demonstrated that higher loading can be achieved without leading to larger-scale separations. Similarly, the effects of non-axisymmetric endwall contouring on a low-speed tandem stator were investigated, resulting in efficiency improvements, particularly under near-stall conditions [11]. Despite this considerable research, the application of air injection strategies within tandem aerofoil systems remains underexplored.

Building on these insights, the current study seeks to unveil new opportunities by numerically investigating air injection in the endwall region of a tandem stator setup, aiming to unlock the full potential of tandem vanes in a highly-loaded axial compressor. The study is performed in two steps: Identification of the primary loss sources within the assembly using numerical analysis of the reference compressor stage followed by a design of the optimum geometry of air injection slots and study of the impact of injection sites on stator and stage performance. Given the limitations imposed by the shrouded cavity at the hub, which complicates the implementation of flow control measures in that region, the focus of this study is justifiably placed on the endwall near the casing.

1 COMPRESSOR REFERENCE CASE

For the current study, a 3.5-stage low-speed research compressor was adopted as the reference geometry [12]. This research compressor, situated at the Institute of Turbomachinery and Flight Propulsion of the Technical University of Munich (TUM), is designated for future experimental investigations. The numerical study focuses on the front 1.5-stage, which comprises an Inlet Guide Vane (IGV), a Rotor, and a Tandem Stator. The tandem stator consists of front and rear vanes (S1, S2) featuring a shrouded cavity arrangement. Table 1 summarizes key compressor parameters for the 1.5-stage setup.

Table 1
Reference Parameters for the Low-Speed 1.5-Stage Compressor

Number of blades IGV/Rotor/S1/S2	40/40/40/40
Solidity at mid span IGV/Rotor/S1/ S2	1.00/1.49/1.10/0.87
Design Rotational speed [RPM]	1484.85
Design Mass flow rate [kg/s]	17.922
Hub-to-tip ratio [-]	0.8
Rotor tip gap clearance [%]	1.75
Cavity clearance [%]	0.95
Design flow coefficient [-]	0.57
Design work coefficient [-]	0.58
Design Π_{tt} [-]	1.03758
Design $\eta_{tt,pol}$ [%]	88.67

2 INJECTION SLOT PARAMETERS

The design of the selected injection slot geometry is based on the Coandă effect [13]. The Coandă effect is the tendency of fluid streams to follow curved surfaces due to viscosity and pressure drop as the fluid accelerates along curved surfaces, with a pressure gradient-induced centripetal force that ensures sustained adherence. This type of injector is recognized for its non-intrusive application in multistage compressors, capable of generating a wall jet with significant axial velocity along the compressor casing, as documented in [14]. The slots are strategically positioned within the stator row on the casing and are uniformly distributed pitchwise, numbering a total of 40, to ensure even flow distribution. Figure 1 presents a standard injector geometry and its key geometrical parameters.

The key parameters for the injection slots include: the circumferential width w_c, the width at the injector inlet $w_{a,inlet}$, the width at the interface injector-casing $w_{a,interface}$, the radius of curvature R_c, the injection mass flow rate $\dot{m}_{inj}$, the slot inclination angle α measured near the injector outlet, the jet angle β, and the normalized chordwise location ζ. As shown in Figure 1, the jet angle β is defined as the angle between the injector outlet and the local tangent to the blade surface at the injection point. This angle is crucial for understanding how the injected fluid is oriented relative to the blade. A β of 0° indicates a parallel orientation of the injection direction with the blade at the injection location. Meanwhile, positive β values direct the injection towards the blade, and negative values direct it away from the blade. The dimensionless parameter ζ represents the injection location along the blade chord, normalized from 0 at the leading edge to 1 at the trailing edge for the front vane, and from 1 to 2 for the rear vane. Thus, for the front vane:

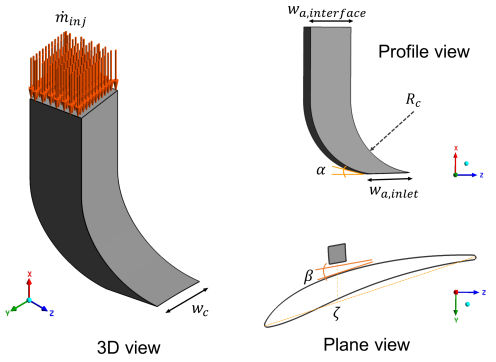

Figure 1: Standard injector geometry and its main geometrical parameters. The plane view details the interface of the injector with the casing and its alignment relative to the blade, highlighting the jet angle β.

$$\zeta = z \qquad \text{(for the front vane)}$$
$$\zeta = 1 + z \qquad \text{(for the rear vane)}$$

with z being the respective chord fraction at the injection location.

3 SIMULATION SETUP

For the numerical study, only one pitch along the 1.5-stage configuration is considered, and all numerical simulations were performed under a steady-state regime using Ansys CFX 2021 R1 as the fluid solver. In the simulation, boundary conditions were defined with a predetermined radial distribution of total pressure and flow direction characterized by a turbulence fractional intensity of 0.05. The total pressure distribution at the inlet was reduced at the upper and lower 20% to mimic the increase in boundary layer thickness seen in prior stages, as the examined stage was designed to fit aerodynamically into the latter part of a high-pressure compressor stage that operates under high load. Additionally, the inlet total temperature was established at 288 K. For the outlet boundary conditions, the mass flow rate was imposed, adjusting this value for the different operating conditions. The fluid was modeled as an Air Ideal Gas, while the turbulence model utilized was the Shear Stress Transport (SST) model. This choice was in alignment with the findings presented in [7] for a similar low-speed compressor. To ensure effective solver control, a high-resolution model was adopted for both

the advection scheme and turbulence. The interfaces between Rotor-IGV and Rotor-Tandem Stator were modeled using a mixing plane, while the interfaces of the shrouded cavity and Tandem Stator used full non-matching boundaries and Frozen Rotor as the mixing model. The meridional view of the 1.5-stage setup is presented in Figure 2, with some details of the interfaces and boundary conditions used for the CFD simulations.

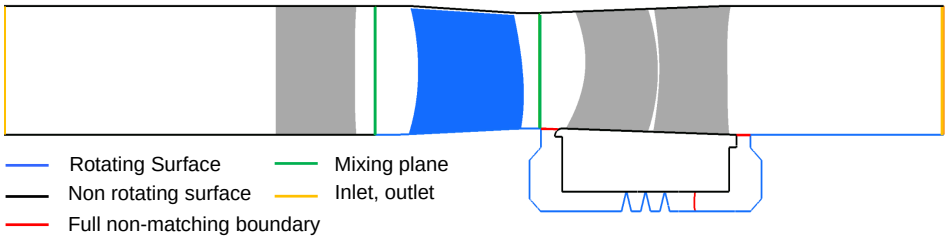

Figure 2: Meridional view of the reference low-speed 1.5-stage axial compressor.

On the other hand, the injection slot within the stator casing was designed with CATIA V5. For its inlet boundary conditions, the injection mass flow rate and total temperature were specified. The casing and the injection slot were connected through a non-conformal interface using a General Grid Interface (GGI). GGI connections, as implemented in ANSYS CFX, facilitate conservative and implicit connections of non-matching meshes, allowing for differences in node locations, element types, and surface extents [15].

Convergence was considered attained when the coefficient of variance (CoV) of polytropic stage efficiency, total pressure ratio, and inlet mass flow rate all reached magnitudes on the order of 1×10^{-5}, assuring the normalized residuals are below 1×10^{-5} and imbalances below 1×10^{-3}.

The mesh for the 1.5-stage compressor was created using Autogrid5$^{\text{TM}}$ version 17.1 [16]. A structured grid employing a conventional O4H topology and standard quality criteria was applied, setting the cell size closest to the wall at 3×10^{-6} m, corresponding to a dimensionless wall distance of $y^+ \approx 1$. For the slot, ICEM CFD was utilized to develop a structured grid. Additionally, the region in the casing around the interface with the injector was refined to enhance precision. The final grid resolutions for both the reference compressor and the refinement area where the injector is placed were determined through a mesh independence study, following standard guidelines [17], to ensure accurate and mesh-size independent results. The study considered parameters such as the stage total pressure ratio (Π_{tt}) and Total Pressure (P_t) at the Stator Outlet for the 1.5-stage setup, along with the mass flow rate ($\dot{m}_{inj}$) for the injector, as detailed in Table 2.

The mesh for the 1.5-stage compressor, created using Autogrid5$^{\text{TM}}$ version 17.1 [16], employed a structured grid with a conventional O4H topology and standard quality criteria, featuring a near-wall cell size of 3×10^{-6} m ($y^+ \approx 1$). A structured grid was also developed for the slot using ICEM CFD. Additionally, the region in the casing around the interface with the injector was refined to enhance precision. The final grid resolutions were determined via a mesh independence study, following the methodology and notation in [17]. According to these guidelines, the Grid Convergence Index (GCI) method was used to quantify numerical uncertainty, indicating the estimated error percentage in the computed results due to mesh discretization. Low GCI values imply a high confidence level in the accuracy of the results, suggesting minimal sensitivity to further mesh refinement. The parameters assessed include the stage total pressure ratio (Π_{tt}), total pressure (P_t) at the stator outlet, and the injection mass flow rate ($\dot{m}_{inj}$), as detailed in Table 2.

The final selected mesh comprises approximately 9.83 M (million) cells, divided among 1.46 M for the IGV, 1.49 M for the rotor, 4.05 M for the Tandem Stator (TS), and 2.83 M for the shrouded cavity of the compressor. Approximately 0.5 M cells are allocated to the refinement area to ensure sufficient resolution. For a

Table 2
GCI Study Results

	$\phi = \Pi_{tt}$ [-]	$\phi = P_t$ [Pa]	$\phi = \dot{m}_{inj}$ [kg/s]
$N1, N2, N3$[M]	22.78, 9.83, 3.91	22.78, 9.83, 3.91	0.053, 0.46, 1.79
r_{21}	1.323	1.323	1.57
r_{32}	1.36	1.36	2.05
ϕ_1	1.03754	104915	0.001355
ϕ_2	1.03758	104916	0.001362
ϕ_3	1.03769	104919	0.001392
p	3.1	3.39	7.61
ϕ_{ext}^{21}	1.037511	104914.37	0.0013933
e_a^{21}	0.00386%	0.000953%	2.124 %
e_{ext}^{21}	0.00279%	0.000602%	0.071 %
GCI_{fine}^{21}	0.00349%	0.000752%	0.088 %

standard injector geometry with a width of 6 mm, the model incorporates at least 0.3 M cells, with this number proportionally increasing for larger widths. Figure 3 provides an overview of the mesh for the Tandem Stator with one standard injector positioned at the casing. The zoomed-in view details the mesh of the injector and the refinement in the casing region.

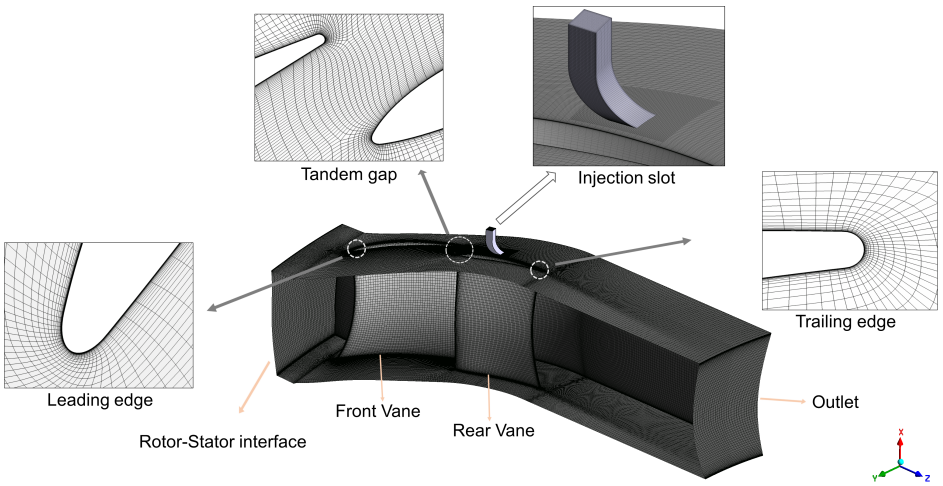

Figure 3: Overview of the mesh for the Tandem Stator with an injector slot, highlighting the mesh refinement within the stator casing.

4 RESULTS AND DISCUSSION

In this section, we present the outcomes of our analysis, focusing on key performance indicators. It is important to note that unless explicitly stated otherwise, all variables mentioned herein refer to their mass flow-averaged values. Specific instances or locations where non-averaged or instantaneous values are considered will be clearly identified.

4.1 Smooth Casing Case

This section examines the aerodynamic performance of the compressor in its baseline configuration, termed the smooth casing (SC) case. It focuses on characterizing the foundational performance aspects of the reference stage. In Figure 4, the speedline for the reference stage is presented, showing the mass flow averaged total-to-total polytropic efficiency ($\overline{\eta}_{\mathrm{tt}}$) and the mass flow averaged total-to-total pressure ratio ($\overline{\Pi}_{\mathrm{tt}}$), plotted against the normalized mass flow rate with respect to the design point mass flow rate ($\dot{m}/\dot{m}_{\mathrm{DP}}$), differentiating between Stage and Rotor. At the design point, the stage achieves a total pressure ratio $\overline{\Pi}_{\mathrm{tt}}$ of 1.0376, a polytropic efficiency $\overline{\eta}_{\mathrm{tt}}$ of 88.65%, and an inlet corrected mass flow $\dot{m}_{\mathrm{DP}}$ of

17.922 kg s^{-1}. The analysis reveals that the compressor operational range is constrained, with stall anticipated at approximately 85% of $\dot{m}_{\mathrm{DP}}$ and a stall mass flow rate of 15.1 kg s^{-1}. The rotor performance significantly influences the overall stage behavior, dominated by a double-leakage tip clearance flow [12]. Accordingly, the current study focuses on stator endwall injection to enhance performance primarily at the design point rather than expanding the stall margin. Figure 5 presents

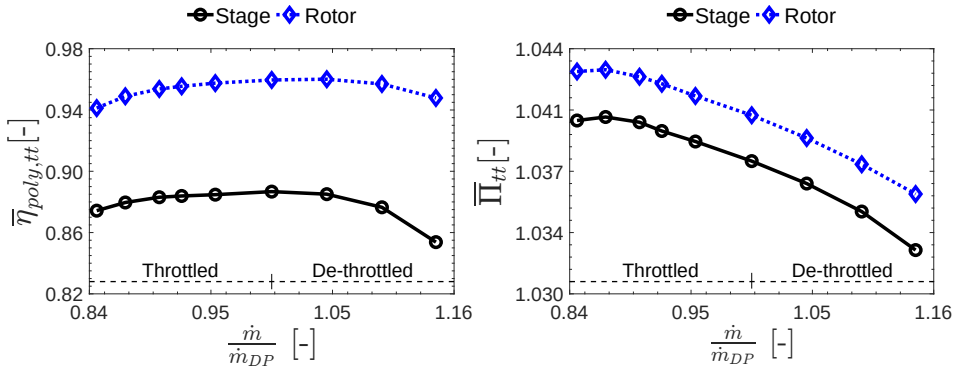

Figure 4: Speedline showing mass flow averaged total-to-total polytropic efficiency ($\overline{\eta}_{\mathrm{tt}}$) and pressure ratio ($\overline{\Pi}_{\mathrm{tt}}$) for the compressor stage and rotor.

normalized spanwise mass-averaged profiles of key aerodynamic parameters within the stator: the static pressure rise coefficient $\overline{C_p}$, total pressure loss coefficient $\overline{\omega}$, and the axial velocity $\overline{u_z}$ at both the leading and trailing edges, plotted alongside the stage polytropic efficiency $\overline{\eta}_{\mathrm{tt}}$ profile.

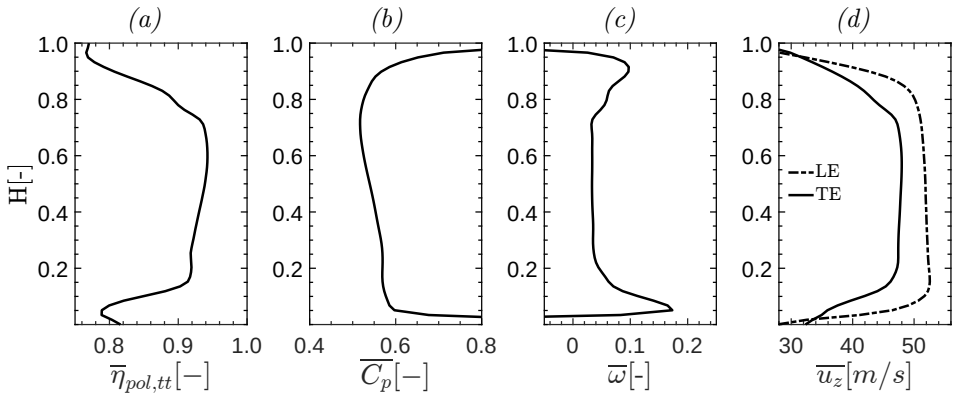

Figure 5: Normalized spanwise profiles at design point : (a) stage efficiency $\overline{\eta}_{\mathrm{tt}}$, (b) stator $\overline{C_p}$, (c) stator $\overline{\omega}$, and (d) axial velocities $\overline{u_z}$ at the leading edge and trailing edge of the stator vanes.

As observed, the total pressure loss coefficient exhibits a pronounced increase towards the casing, correlating with the efficiency drop and indicating significant aerodynamic losses. This increase is consistent with the abrupt rise in $\overline{C_p}$ over 80% span, suggesting a rapid conversion of dynamic pressure into static pressure. The axial velocity profiles further reinforce these observations, with reduced velocities at the stator trailing edge near the casing starting at $H = 0.7$, contrasting with the less pronounced velocity reduction at the leading edge, beginning at about $H = 0.85$. This pattern suggests a growth in the boundary layer thickness, influenced by adverse pressure gradients, leading to the deceleration of fluid particles which can precipitate flow separation. Additionally, the blockage from upstream rotor tip leakage contributes to low momentum flow, further impacting stator performance. Although similar phenomena are observed near the hub locations, we omit their discussion since the focus is placed on the near-casing endwall region.

The flow behavior over the blade surfaces can be examined in Figure 6. The blade loading profiles of the isentropic Mach number ($\mathrm{Ma}_{\mathrm{is}}$) are shown at two critical spanwise locations: mid-span ($H = 0.5$) and near the casing ($H = 0.9$), together with the limiting streamlines and static pressure contour. There is a pro-

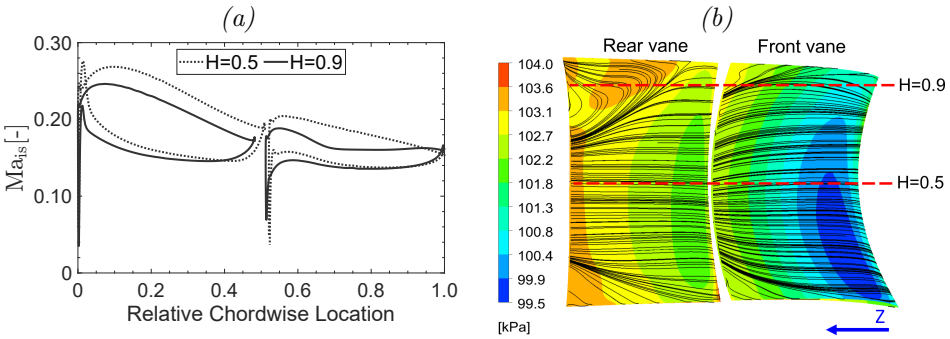

Figure 6: (*a*) Isentropic Mach number profiles at mid-span ($H = 0.5$) and near the casing ($H = 0.9$); (*a*) Limiting streamlines and static pressure contour on the Tandem Stator suction side.

nounced loading on the front vane compared to the rear vane, suggested by the greater separation between the suction and pressure sides of the front vane. This is confirmed by an overall diffusion factor (DF) of 0.52 considering an equivalent chord, while the independent DF values for the front and rear vanes are 0.44 and 0.27, respectively. At $H = 0.5$, the $\mathrm{Ma_{is}}$ profiles exhibit smooth gradients for both blade profiles and consistently higher loading along the chord length compared to $H = 0.9$. This contrast suggests the influence of three-dimensional effects and endwall interactions. The rear vane exhibits a flattening at the suction side of the $\mathrm{Ma_{is}}$ profile around the 0.7 chordwise location for $H = 0.9$, leading to a localized reduced diffusion capacity due to flow detachment. The limiting streamlines at the suction side of the rear vane confirm the near-casing corner separation, correlating with the restrained increase in static pressure. Such complicated nature of secondary flow effects at the endwall region in tandem configurations has been previously attributed to the interaction between the front and rear vanes [18].

These findings imply that the aerodynamic performance can be further improved, potentially through targeted flow control strategies. The subsequent sections will discuss the implementation of endwall injection as a means to address these identified shortcomings and thereby improve the stator and stage performance.

4.2 Baseline injection case

A baseline injection case to conduct parametric studies on various geometrical variables is considered. The anticipated flow separation zone on the suction side of the rear vane (RV) suggests that locations on the suction side of the rear vane are promising for flow energization via air injection. Accordingly, the baseline location for air injection has been selected at roughly 40% of the rear vane chord length. Following the definition presented in Section 2, the normalized chordwise location, denoted by ζ, is set to 1.4. Table 3 outlines the preliminary design space parameters and the values selected for the baseline case. The injection temperature, $\mathrm{T_{inj}}$, is set at 294 K, reflecting the mean fluid temperature across the compressor. This assumption is justified, considering the injection source is typically derived from later stages, a methodology consistent with previous parametric studies on injection [19]. To ensure minimal disturbance to the main flow, initial values are chosen conservatively. In light of prior research [20], minimizing injection angles is critical; hence, the adoption of relatively low α values. The initial injection jet is aligned tangentially with the blade at the injection location ($\beta = 0$). To minimize losses in efficiency, it is preferable to keep the injection mass flow rate to a minimum [21]. The injection mass flow rate is normalized with respect to the stall mass flow rate ($\mathrm{\dot{m}_{inj}/\dot{m}_{stall}}$), where $\dot{m}_{stall}$ represents the minimum mass flow rate the compressor stage can handle before reaching stall conditions and is a fixed parameter for the smooth casing case, approximately $15\,\mathrm{kg\,s^{-1}}$. The initial widths of the injector are equivalent to the average thickness of the blade, being specified as 6 mm.

In our study, we selected an exit Mach number for the injector ($\mathrm{Ma} \approx 0.35$),

Table 3
Design Space Parameters and Baseline Values.

Parameter	Design space	Baseline
$\boldsymbol{\zeta}$ [-]	[0.1, 1.7]	1.4
$\mathbf{T_{inj}}$ [K]	Constant	294
$\boldsymbol{\alpha}$ [°]	[2.5, 10]	5
$\boldsymbol{\beta}$ [°]	[-15, 45]	0
$\mathbf{R_c}$ [mm]	[5, 12.5]	10
$\mathbf{w_c}$ [mm]	[6, 12]	6
$\mathbf{w_{a,inlet}}$ [mm]	Constant	6
$\mathbf{w_{a,interface}}$ [mm]	Constant	6
$\boldsymbol{\dot{m}_{inj}/\dot{m}_{stall}}$ [%]	[0, 1]	0.5

which falls within the range of the maximum Ma observed in the compressor, to ensure a realistic operational context. This conservative approach avoids to induce high-speed flow phenomena that could compromise flow stability and aerodynamic integrity. The injector exit Ma number is considered an upper limit for the parametric study.

4.3 Injector Parametric Study

Initially, we examine the isolated impacts of key injection parameters such as the inclination angle (α), jet angle (β), and radius of curvature (R_c), keeping the normalized chordwise location (ζ) at 1.4. After establishing optimal values for α, β, and R_c, our focus shifts to assess the interaction between the circumferential width ($\mathrm{w_c}$) and the relative injection mass flow rate with respect to the stall mass flow rate ($\mathrm{\dot{m}_{inj}/\dot{m}_{stall}}$), given their combined influence on achieving the desired exit injector Mach number within specified limits. This process refines our baseline towards an enhanced configuration. Finally, we explore variations in ζ values to determine effective injector locations.

The subsequent figures illustrate the influence of injection parameters on key aerodynamic performance metrics, showing variations (Δ) for increments in stage variables such as polytropic efficiency η_{tt} and total pressure ratio Π_{tt}, defined as follows:

$$\eta_{\mathrm{tt}} = \frac{\ln\left(\frac{P_{t2}}{P_{t1}}\right)}{\ln\left(\frac{T_{t2}}{T_{t1}}\right)} \tag{1}$$

$$\Pi_{\mathrm{tt}} = \frac{P_{t2}}{P_{t1}} \tag{2}$$

where P_{t2} and P_{t1} are the total pressures at the outlet and inlet, respectively, and T_{t2} and T_{t1} are the corresponding total temperatures. The percentage variation Δ for any performance metric, such as η_{tt} or Π_{tt}, is calculated using the formula:

$$\Delta = \left(\frac{\phi_{\mathrm{inj}}}{\phi_{\mathrm{smooth}}} - 1\right) \times 100\% \tag{3}$$

where ϕ_{inj} represents the value of the variable for the injection case, and ϕ_{smooth} represents the value for the smooth casing case.

These parameters are evaluated as mass-flow averaged values at specific axial locations: the rotor inlet and stator outlet. The analysis utilizes standard definitions, primarily focusing on the aerodynamic impacts without directly accounting for the costs associated with injection. However, the influence of the injected flow is inherently captured in the outlet conditions, affecting the polytropic efficiency and total pressure ratio. This relationship is further explored through the use of the momentum coefficient C_u, which correlates with the aerodynamic performance improvements observed. Detailed consideration of injection losses, including the total pressure loss coefficient ω_t, is discussed in Section 4.8, where a more com-

prehensive evaluation includes the mass flow rates of both the main and injected flows.

4.3.1 Influence of inclination angle

Figure 7 demonstrates how the injector slot inclination angle α affects aerodynamic performance, indicating that a lower α significantly enhances stage efficiency. Specifically, an angle of $\alpha = 2.5°$ was found to yield optimal performance enhancements, with increases in η_{tt} and Π_{tt} of 0.463% and 0.037%, respectively. A lower injection angle typically correlates with a more tangential introduction of flow. This implies a less disruptive influence on the main flow, potentially allowing for a smoother integration of the injected air with the primary flow path, as found in [3].

However, from a numerical perspective, angles approaching zero can present significant challenges in maintaining mesh quality, particularly after a curvature in the flow path. Poor mesh quality, characterized by skewed or highly stretched cells, can introduce numerical inaccuracies and make it difficult to achieve stable and accurate CFD simulations. From a design perspective, very low angles may require higher injection pressures to overcome flow resistance, complicating the injection system design. Therefore, an angle of 5° represents a balanced compromise, ensuring sufficient mesh quality while enhancing aerodynamic performance.

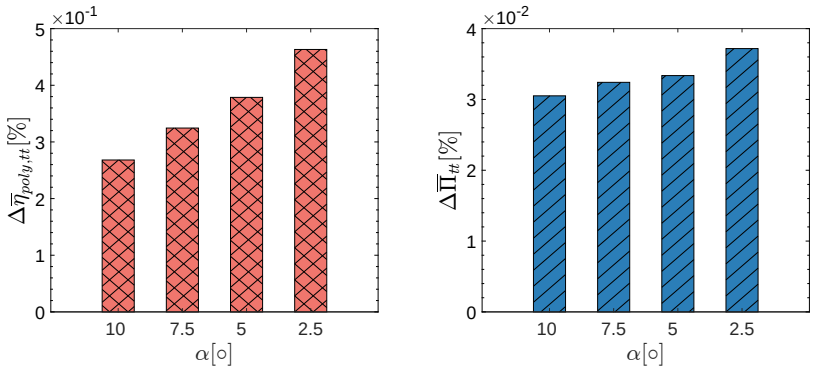

Figure 7: Impact of the injector inclination angle α on aerodynamic performance.

4.3.2 Influence of jet angle

Analysis of aerodynamic performance relative to jet angle (β) reveals that maintaining β within a range of approximately 0° to 20° maintains higher efficiency and pressure ratio increments, with a peak in η_{tt} increment at $\beta = 5°$ of about 0.385%. Conversely, excessively large or negative jet angles fall outside this suitable range, potentially disrupting the flow and reducing performance. The variability in η_{tt}, indicated by a CoV of 0.220, and the less sensitive changes in Π_{tt} (CoV of $\Pi_{\mathrm{tt}} = 0.076$), highlight the importance of smoothly directing the injected flow towards the suction side of the rear vane to integrate it with the endwall region flow. Figure 9 displays 3D velocity streamlines and blade limiting streamlines with static pressure contours for $\beta = 45°$, 5°, and $-15°$, demonstrating ineffective flow separation zone control at β values outside the optimal range. While $\beta = 5°$ represents an identified peak in performance, a broader range of jet angles around this value can also achieve desirable outcomes, depending on the specific blade geometry and its relation to the critical flow separation zone. This relationship can vary along the chordwise direction, necessitating adjustments in the jet angle to effectively target the problematic regions.

4.3.3 Influence of radius of curvature

The impact of the injector radius of curvature (R_c) on injection effectiveness is demonstrated in Figure 10, where an increase in R_c aligns with improved injection efficacy, consistent with the findings of [1]. Optimal performance is achieved at $R_c = 12.5$ mm, which corresponds to peak increments in η_{tt} (0.455%) and Π_{tt} (0.039%). For a Coanda-type injector, a larger curvature promotes sustained flow attachment on the convex side, enhancing flow acceleration due to the induced

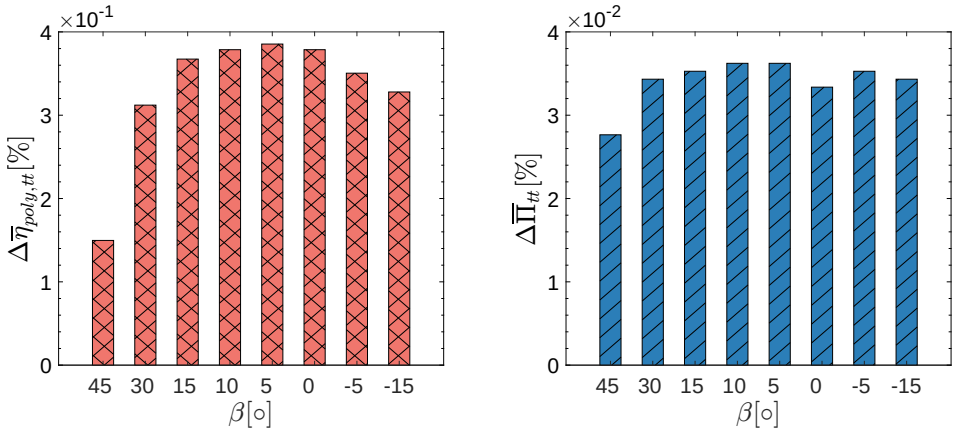

Figure 8: Sensitivity of jet angles to aerodynamic parameters.

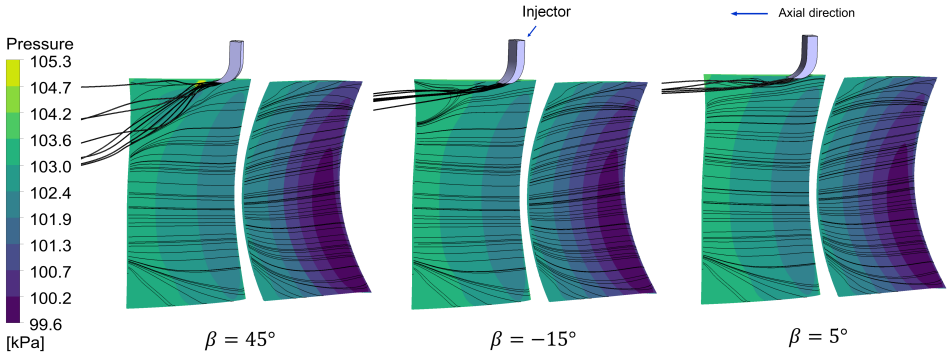

Figure 9: Blade limiting streamlines with static pressure contours and 3D injector velocity field for different β angles.

radial pressure gradient [22]. This results in a high-momentum jet that mitigates separation zones and enhances flow mixing.

As R_c increases, the injector can maintain a higher exit velocity, similar to the effect of decreasing the injection inclination angle (α). A stronger curvature allows the flow to accelerate more effectively, thereby enhancing the momentum coefficient (C_u), which will be defined in the next section. In this study, larger values of R_c beyond 12.5 mm were not explored, as they resulted in exit velocities exceeding the specified limits. Additionally, an increase in R_c typically requires higher injection pressures to overcome the associated increase in flow resistance.

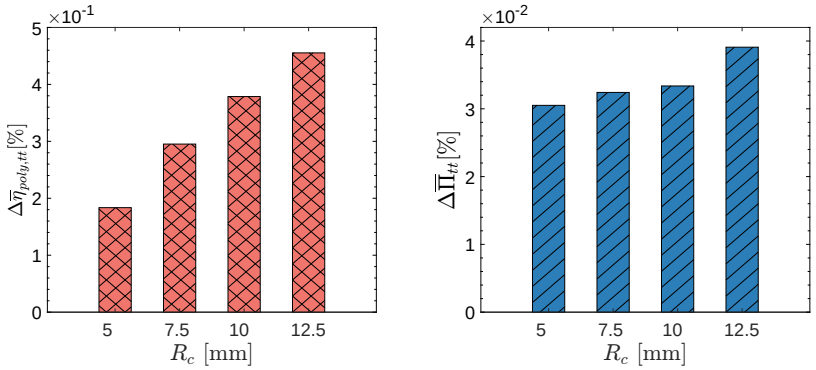

Figure 10: Aerodynamic influence of the injector radius of curvature R_c.

4.3.4 Role of momentum coefficient

For the variables circumferential width (w_c) and relative injection mass flow rate ($\dot{m}_{\text{inj}}/\dot{m}_{\text{stall}}$), their combined influence on aerodynamic performance is analyzed due to their strong interrelated effects. From a physical standpoint, an increase in $\dot{m}_{\text{inj}}/\dot{m}_{\text{stall}}$ with unchanged geometry leads to higher velocity and momentum.

Conversely, an increase in w_c at a constant $\dot{m}_{\text{inj}}$ reduces it. Thus, establishing an optimal balance between w_c and $\dot{m}_{\text{inj}}/\dot{m}_{\text{stall}}$ is crucial for enhancing injection performance.

To this end, we introduce the so-called Refined Configurations, featuring varying circumferential widths (w_c) to examine the interaction between w_c and $\dot{m}_{\text{inj}}/\dot{m}_{\text{stall}}$. Accordingly, the inclination angle (α) is set at 5° to strike a balance between aerodynamic advantages and mesh quality. The optimal jet angle (β) of 5° was determined based on its standout performance in preliminary analyses. Moreover, the radius of curvature (R_c) is fixed at 12.5 mm, aligning with the most favorable outcomes. Assumptions for other parameters remain as specified in the baseline scenario. Details of these configurations are presented in Table 4, exploring a spectrum of w_c values to evaluate their effects within the predefined $\dot{m}_{\text{inj}}/\dot{m}_{\text{stall}}$ ranges, selected with consideration for the injector exit Mach number restrictions.

Table 4
Parameters for refined injection configurations.

	Ref$_1$	**Ref$_2$**	**Ref$_3$**	**Ref$_4$**
$\boldsymbol{w_c}$ **[mm]**	6	8	10	12
$\boldsymbol{\dot{m}_{\text{inj}}/\dot{m}_{\text{stall}}}$ **[%]**	[0.2,0.45]	[0.4,0.6]	[0.5,0.75]	[0.6,0.9]

To characterize each injection case, the momentum coefficient [23], defined as the ratio of the blowing-flow momentum flux to the free-stream momentum flux, is represented in Equation 4:

$$C_u = \frac{u_{inj}^2 \cdot w_c}{0.5 \cdot u_\infty^2 \cdot c} \cdot \sin(\beta) \tag{4}$$

where C_u is the momentum coefficient, u_{inj} is the velocity of the blowing flow, w_c is the width of the blowing slot, u_∞ is the free-stream velocity, c is the chord length of the blade, and β is the blowing (jet) angle. The value for c is considered to be the equivalent chord of the blade in the tandem stator, measured from the leading edge of the front vane to the trailing edge of the rear vane.

Figure 11 illustrates the effects of the refined configurations on aerodynamic parameters for different injection ratios. At a fixed $\dot{m}_{\text{inj}}/\dot{m}_{\text{stall}}$, a smaller w_c yields better injection effectiveness, whereas at a constant w_c, a higher $\dot{m}_{\text{inj}}/\dot{m}_{\text{stall}}$ enhances performance. Judging by the gains in polytropic efficiency and total pressure ratio, Ref$_4$ emerges as a strong configuration, achieving the highest increments at the peak $\dot{m}_{\text{inj}}/\dot{m}_{\text{stall}}$ value (0.49% for η_{tt} and 0.056% for Π_{tt}). For similar aerodynamic gains, minimizing injection rates can be compensated by decreasing circumferential widths.

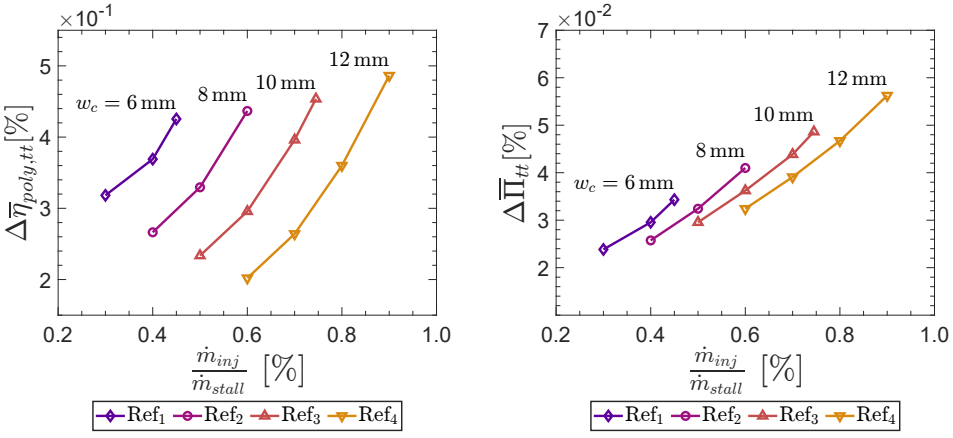

Figure 11: Interplay of w_c and $\dot{m}_{\text{inj}}/\dot{m}_{\text{stall}}$ on aerodynamic performance.

The equivalent momentum coefficients C_u are plotted in Figure 12 against the ratio u_{inj}/u_∞, together with a colormap to show the gains in efficiency and total pressure ratio for each case. The analysis reveals findings similar to those in

[23]. In that work, an analytical model was proposed to predict the effectiveness of steady blowing for boundary layer control, assuming that both the main flow and the blowing flow are incompressible and have the same density. For the current low-speed compressor setup, these assumptions are considered valid. The study found that a reduction in the momentum thickness of the boundary layer correlates with the momentum coefficient. Relating the reduction of momentum thickness to an improvement in aerodynamic performance, we observed that at a constant momentum coefficient and blowing angle, the gain is more pronounced with higher blown-to-free stream velocity ratios (lower w_c), as long as the blown flow forward velocity exceeds the free stream velocity. In terms of efficiency, for a constant velocity ratio closer to 1, larger C_u values represented by larger widths are not beneficial. Conversely, for u_{inj}/u_∞ closer to 2, the improvement correlates proportionally with the momentum coefficient, as can be seen when comparing the peak cases of every configuration. In terms of the total pressure ratio, higher momentum flow correlates with higher pressure ratio values for every case of velocity ratio, since we are introducing a higher energy fluid to the main flow.

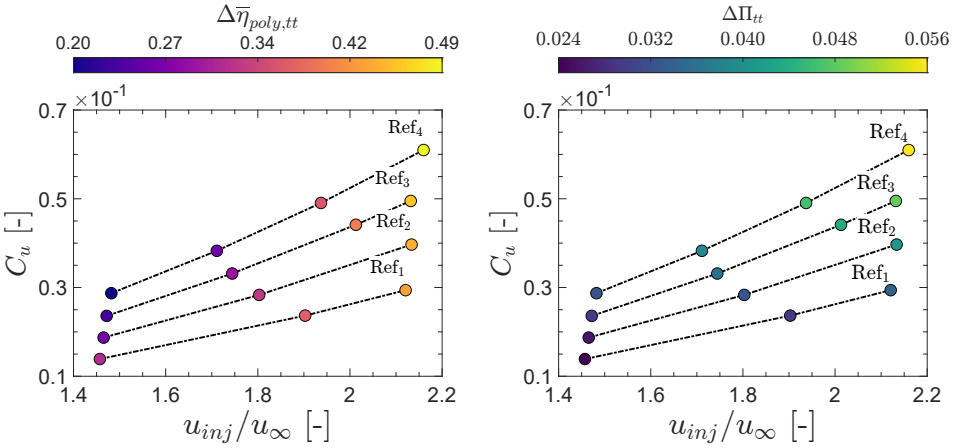

Figure 12: Relationship of C_u and u_{inj}/u_∞ with aerodynamic performance.

4.4 Enhanced Configuration

To ensure comparability across different study locations, it is critical to maintain uniform circumferential widths (w_c). Given the circumferential space constraints in the Tandem Stator gap region, w_c is selected at 10 mm for consistent application and comparison. Thus, Ref$_3$ (w_c = 10 mm) is chosen as the enhanced configuration, with a peak $\dot{m}_{\text{inj}}/\dot{m}_{\text{stall}}$ value of 0.75%. This configuration demonstrates significant enhancements over the smooth casing case with increments of 0.45% in η_{tt} and 0.049% in Π_{tt}.

Span profiles, correlating normalized span H with stage and stator aerodynamic parameters for the smooth casing, baseline, and enhanced configurations, are depicted in Figure 13. The enhanced configuration outperforms in improving stage efficiency and total pressure ratio, especially near the casing, with the injection effect evident downstream of the injection site above $H = 0.6$. Flow redistribution due to injection slightly influences behavior beyond the casing endwall region. Accordingly, the static pressure rise coefficient C_p for both injection cases is above the smooth casing at the regions near the casing and also at mid and lower span zones with less pronounced differences. Specifically, for $H < 0.3$, the near-hub region is minimally affected by the endwall injection. Since there is slightly more pressurized flow in this region for the injection cases, the recirculating flow in the shrouded cavity can slightly increase, marginally raising losses [24]. Nevertheless, the overall impact of the injection remains beneficial.

Furthermore, the entropy contours at different axial locations and the velocity contour for $H = 0.9$ are displayed in Figure 14 for both the enhanced configuration and the smooth casing cases. It is evident that the areas of high entropy in the casing corner separation region have considerably decreased, resulting in a

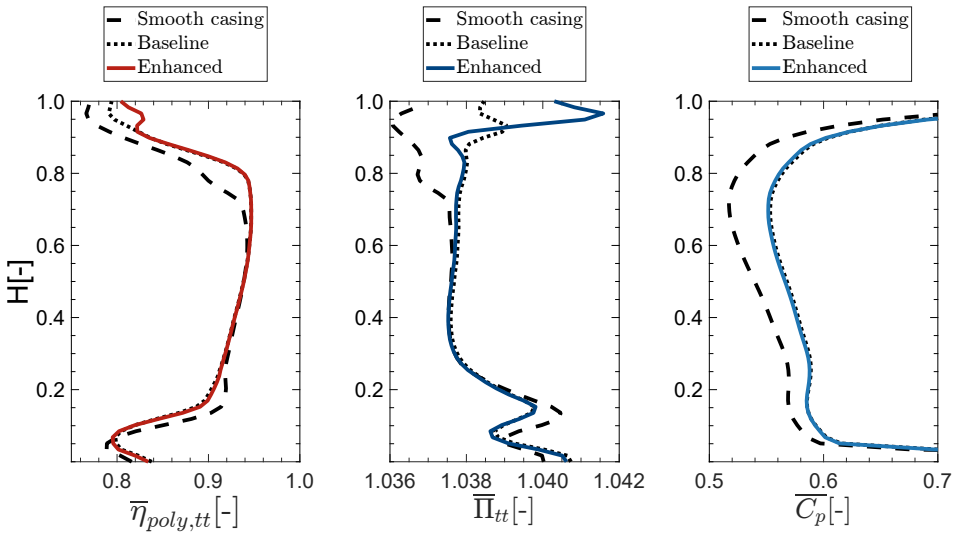

Figure 13: Comparison of span profiles between smooth, baseline, and enhanced configurations. Left: Stage efficiency, middle: Stage total pressure ratio, right: Static pressure rise for the stator.

smoother flow free from vorticity effects. Similarly, the velocity contour near the casing shows a significant reduction in the low-momentum zones. Additionally, the increase in static pressure ratio leads to sliglty more recirculating mass flow in the shrouded cavity, resulting in increased blockage at the stator inlet, as highlighted by the entropy regions near the hub.

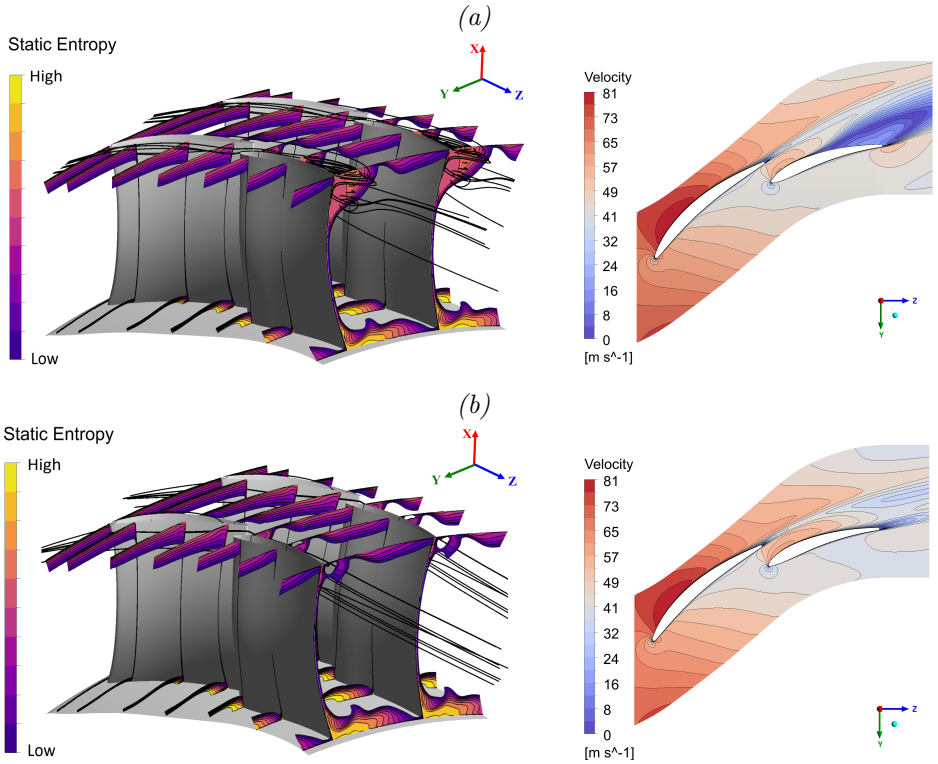

Figure 14: Entropy contours at various axial locations and velocity contour at 90% span. (a) Smooth casing case, (b) Enhanced configuration.

4.5 Effects of injector location

This section examines how the location of the injector affects the aerodynamic performance of the compressor. The analysis focuses on the region along the pressure side of the front vane and the suction side of the rear vane. Areas on the suction side of the front vane and the pressure side of the rear vane were found to

either not improve or negatively impact performance and are therefore not included in this study. Each location was tested using the same enhanced configuration selected in the previous section and maintained the same relative injection mass flow rate $\dot{m}_{\text{inj}}/\dot{m}_{\text{stall}}$. The only variable that changed with the location was the jet angle β, with multiple simulations conducted at each location to identify the optimal angle. Additionally, the same level of mesh refinement for the interface between the injector outlet and stator casing, and the same convergence criteria (as presented in Section 3), were applied across all simulations to ensure consistent results. The final analyzed locations are shown in Figure 15, with the baseline location used in the parametric study highlighted in red.

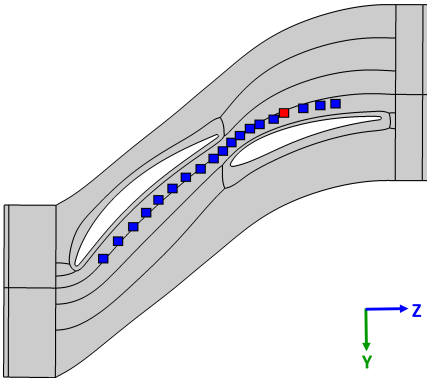

Figure 15: Final injection locations under study. The baseline location is highlighted in red.

The results of the study of injector locations are detailed in Figure 16. The efficiency η_{tt} demonstrated greater variability, with a Coefficient of Variation (CoV) of 24.68%. The maximum increase in η_{tt} is observed at an axial location of 1.2 (20% chord of the rear vane), with an efficiency increment of 0.462%. The analysis indicates that significant performance improvements are attainable in the transition area between the front and rear vanes, especially within the rear vane region. For η_{tt} increments, the optimal range is found to be between ζ values of 1 to 1.4; beyond this, efficiency starts to drop. The total pressure ratio (Π_{tt}) follows a trend very similar to that of η_{tt}. However, it shows lower sensitivity to changes in injector location with a Coefficient of Variation (CoV) of 10.86%, as previously found with other studied injection parameters.

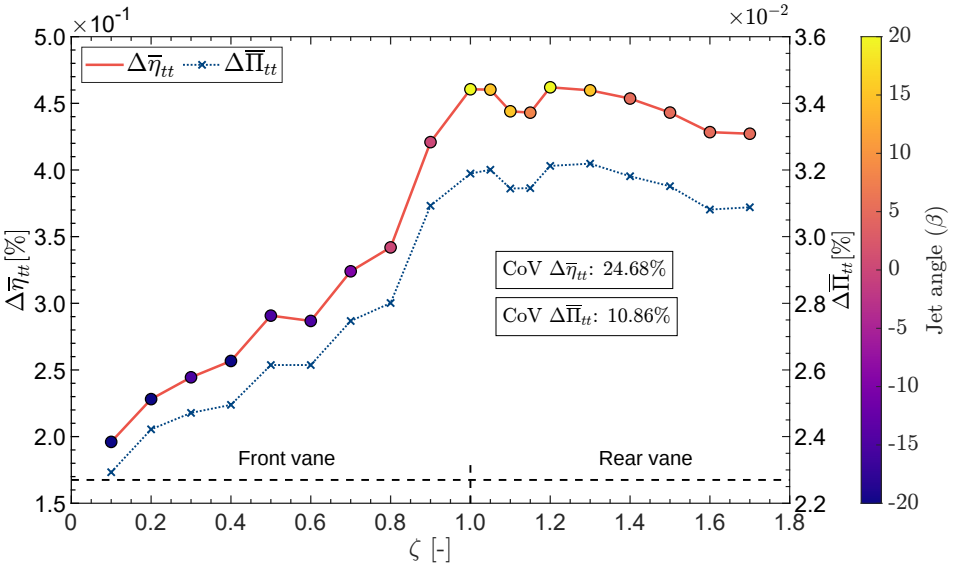

Figure 16: Efficiency and Total pressure ratio variations with injector location. The colormap indicates the jet angle (β), highlighting regions of maximum aerodynamic benefit between the front and rear vanes.

The trend of final jet angles, illustrated by the colormap in Figure 16, emphasizes the need for precise β control across different axial locations to achieve optimal aerodynamic performance. The colormap reveals that front vane injections require negative angles to effectively target flow separation regions at the rear vane, implying a flow direction that slightly opposes the local blade surface tangent. Specifically, the use of negative angles is crucial for improving the flow incidence at the rear vane near the endwall region. This implies that when injec-

tion is performed from front vane locations, it is necessary to effectively adjust the inlet flow angle at the leading edge of the rear vane to efficiently mitigate boundary layer separation at the endwall. Conversely, rear vane injections, situated closer to larger loss regions, necessitate positive angles to address these problematic areas effectively. The required jet angle magnitude is influenced by the injection site proximity to the flow separation region; nearer sites demand smaller angles. For example, an angle of 20 degrees is optimal for $\zeta = 1.2$, reducing to 5 degrees for ζ values beyond 1.4. Figure 17 compares the effect of the optimal jet angle across injection positions at ζ values of 0.5 and 1.2. For $\zeta = 0.5$, the best performance is achieved by directing the flow towards the leading edge of the rear vane; however, since the injection is performed too far from the separation point, the flow diffuses and loses the majority of its momentum. In contrast, for $\zeta = 1.2$, which is a location just upstream of the separation point, the boundary layer is more effectively removed. Such conclusions, previously addressed for configurations with single airfoils [25] , now extend to tandem vanes, offering the first evidence of these effects in published literature.

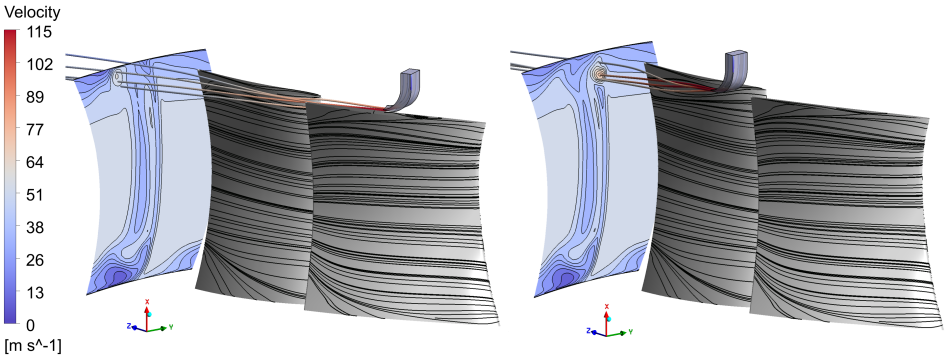

Figure 17: Surface wall and 3D velocity streamlines, alongside the velocity contour at a far axial location from the rear vane for two cases of ζ. The jet angle β changes accordingly to the axial location of the injector

For the subsequent analysis, distinctive cases identified in the study of injection locations are selected. Specifically, two front vane locations at $\zeta = 0.1$ and $\zeta = 0.5$ are chosen to illustrate lower and mid-range performance, respectively. In contrast, rear vane locations at $\zeta = 1.05$ (near the leading edge) and $\zeta = 1.2$ are selected for their notable impacts on η_{tt} and Π_{tt}. Further locations at $\zeta = 1.4$ and $\zeta = 1.6$ are included to characterize behavior at and beyond the separation point. These selections are detailed in Table 5 and will be used for a detailed analysis of span profiles.

Figures 18 and 19 showcase the span profiles for η_{tt} and Π_{tt} for selected injection

Table 5
Selected injection location cases for detailed analysis.

Case Label	Description
Front $\zeta = 0.1$	Least optimal case at the design point
Front $\zeta = 0.5$	Mid-range performance case
Rear$\zeta = 1.05$	Near maximum $\Delta\overline{\eta}_{tt}$, at the leading edge
Rear $\zeta = 1.2$	Maximum efficiency increment case
Rear $\zeta = 1.4$	At the separation point
Rear $\zeta = 1.6$	After separation point

location cases, highlighting divergent behaviors above 85% span. The impact of injection becomes evident beyond 60% span, with all cases showing increased η_{tt} and Π_{tt} compared to the smooth casing scenario. Cases near the rear vane leading edge ($\zeta = 1.05$ and $\zeta = 1.2$) exhibit a uniform and significant increase across a wider span, suggesting enhanced mixing. Specifically, $\zeta = 1.05$ exhibits a consistently

smoother efficiency rise, whereas $\zeta = 1.2$ demonstrates superior performance at lower span values, diminishing towards $H = 1.0$, indicating concentrated injected flow around $H = 0.9$. This distinct profile behavior aligns with the jet angle β for this case, set at 20°. As discussed in Section 4.3, larger β values lead to the injected flow impacting the blade more directly, causing the high-energy flow to shift to lower span zones. For larger ζ values, beyond the separation point, efficiency and total pressure ratio peak near the casing, showing that downstream injection impacts are confined to smaller regions due to diminished mixing. Near the hub, at $H = 0.4$, flow redistribution minimally affects dynamics around the shrouded cavity for all cases.

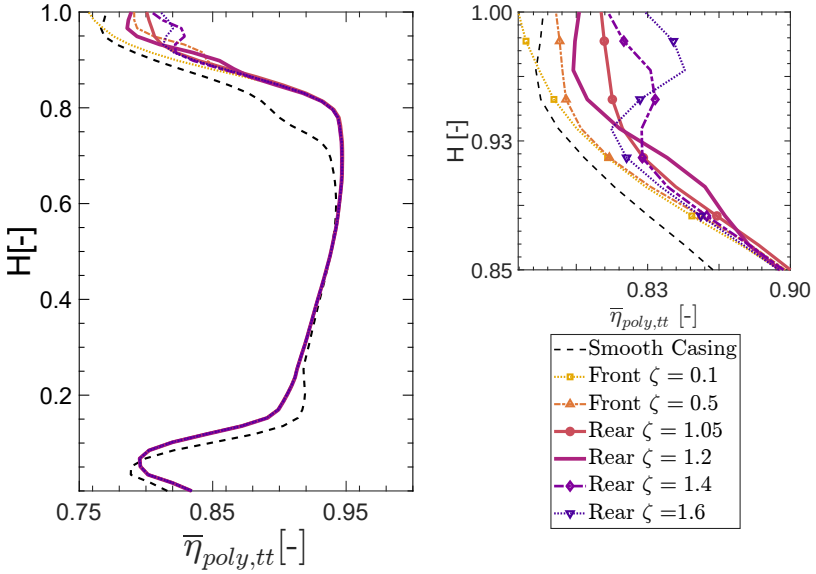

Figure 18: Spanwise distributions of polytropic efficiency for highlighted injection cases. A zoomed-in view shows behavior between H = 0.85 and 1.0.

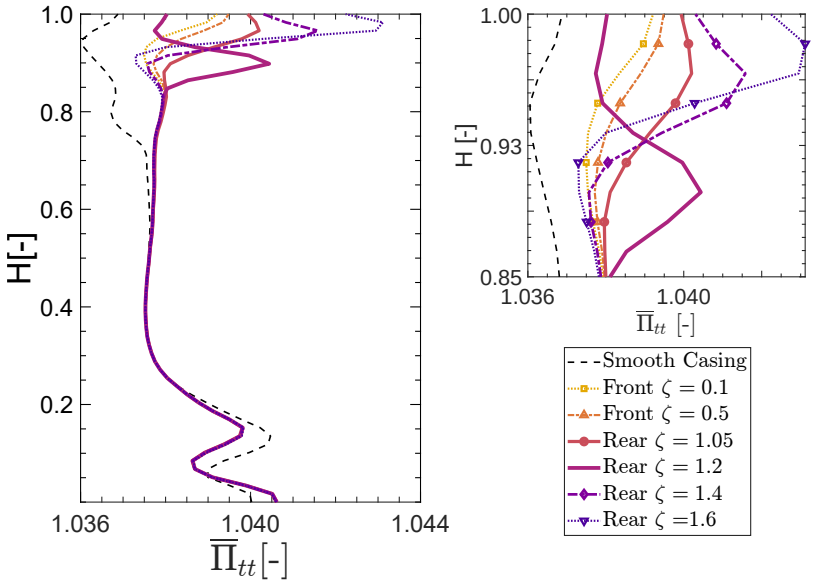

Figure 19: Total pressure ratio (Π_{tt}) profiles with a zoomed-in view, comparing injection cases at different locations.

4.6 Impact at off-design conditions

Finally, we present the impact of the selected configurations under off-design conditions. We maintain the relative injection mass flow rate, $\frac{\dot{m}_{inj}}{\dot{m}_{stall}}$, constant, which leads to variations in the total pressure of the injected fluid across different operational conditions, from de-throttled to stall states for each case. This vari-

ation correlates with an increase in static pressure at the injection site, Π_{static}, typically seen when the injector is fed by downstream flow. Our simulations start at the design point and systematically progress towards de-throttled and stall conditions by incrementally adjusting the exit corrected mass flow rate. Figure 20 showcases the impact of injection location across various operating conditions.

For all injection cases, stage efficiency η_{tt} exceeds that of the smooth casing scenario in Figure 20, demonstrating improved behavior between normalized mass flow rates of 0.9 to 1.1. Beyond this range, the profiles converge and approach the smooth casing curve. Notably, cases near the rear vane consistently outperform those at the front vane across over the entire speedline. Under de-throttled conditions ($\frac{\dot{m}_{\text{inj}}}{\dot{m}_{\text{DP}}} > 1$), efficiency drops are more pronounced for all the cases, specially at those located at $\zeta > 1.2$. At this condition, velocities exceeding those at the design point amplify losses related to boundary layer formation, affecting both vanes [20]. Hence, locations closer to the leading edge offer a balanced approach across various operating conditions. Conversely, the total pressure ratio differences between locations are minimal, with all cases outperforming the smooth casing scenario. It's crucial to note that while injection in the tandem stator does not extend the stall range—predominantly determined by rotor tip flow—it enhances stage performance across the entire operating range.

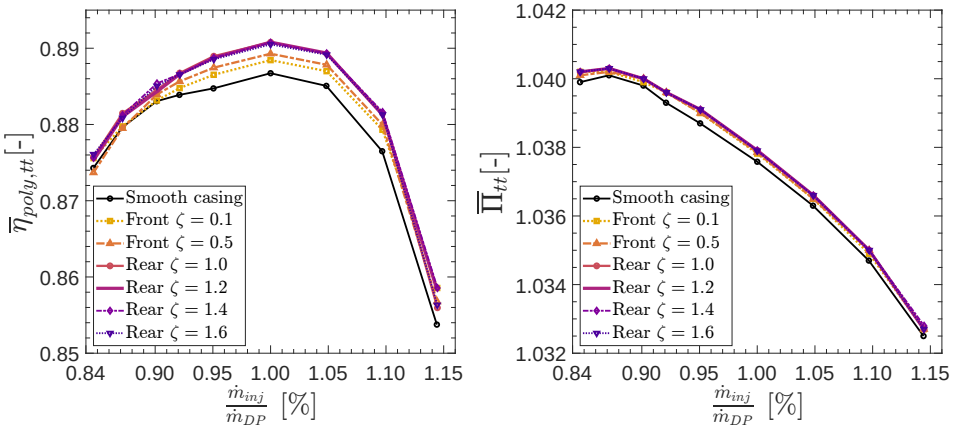

Figure 20: Comparative impact of injection location on polytropic efficiency (left) and total pressure ratio (right) under various operating conditions.

4.7 Injection-Induced Tandem Stator Loading

Given that the highest aerodynamic improvements occur over a range close to the design point, the impact of air injection on blade loading is analyzed at this condition. Figure 21 shows the blade loading at 90% span and profiles for the representative injection case at $\zeta = 1.2$ and the smooth casing case, both at the design point. For stator variables such as turning and flow angle at the stator outlet, mass-flow averaged values are calculated at two axial locations: upstream of the front vane leading edge and downstream of the rear vane trailing edge. As observed in the Ma_{is} curves, the induced loading due to injection is evident in the rear vane when compared against the smooth casing case, demonstrating the removal of corner separation near the casing. This removal of low-momentum flow allows for some unlocking of diffusion capacity in the rear vane. The overall mass-flow averaged diffusion factor DF for this case is 0.54, which is higher than that for the smooth casing case, which is set at 0.521. However, the increase is entirely attributable to the rear vane, with an independent diffusion factor value of 0.29 for the injection case versus 0.27 for the smooth casing scenario. Consequently, an increase in turning for the stator row, alongside the flow angle values at the stator outlet, is observable for $H > 0.6$, indicative of the higher loading effects of injection. Correcting underturning with air injection not only improves blade loading and stage efficiency but also holds promise for enhancing flow incidence for subsequent stages and, therefore, overall efficiency in multi-stage compressors.

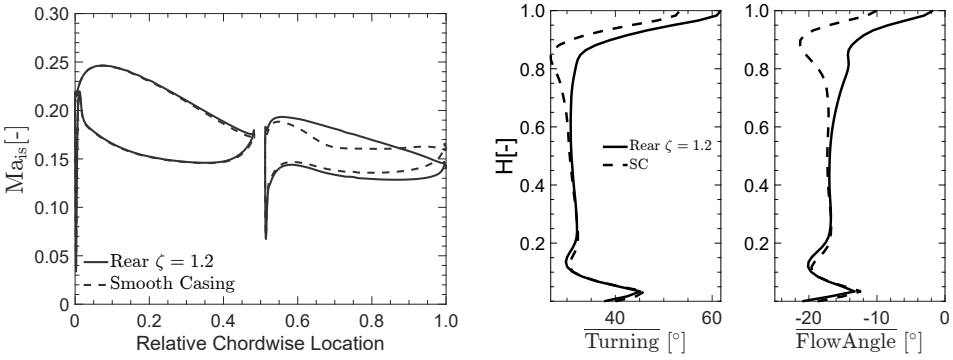

Figure 21: Injection impact on aerodynamic loading. Left: Blade loading profiles at $\zeta = 1.2$ and $H = 0.9$ for injection and smooth casing cases showing the isentropic Mach number. Right: Turning and flow angle at the stator outlet profiles for both cases.

4.8 Injection losses

Throughout this study, our goal was to analyze the aerodynamic impact of injection in a tandem stator configuration and understand how an injection strategy characterized by the momentum coefficient C_u correlates with improvements in stage efficiency and total pressure ratio. Therefore, the source of the injected mass and the potential penalties incurred were not subjects of study. However, in realistic operational conditions, the injection implementation can provoke additional losses in the system.

One common approach to account for total losses, including those from injection, is presented in [21]. According to this study, the total pressure loss coefficient, denoted as ω_t, is defined by a mass-weighted approach that accounts for both the main flow and injected jet contributions. The total pressure loss coefficient is given by:

$$\omega_t = \frac{\dot{m}_1(\overline{P_{t1}} - \overline{P_{t2}}) + \dot{m}_{inj}(\overline{P_{t,inj}} - \overline{P_{t2}})}{\dot{m}_1(\overline{P_{t1}} - \overline{P_1}) + \dot{m}_{inj}(\overline{P_{t,inj}} - \overline{P, inj})} \tag{5}$$

where $\dot{m}_1$ and $\dot{m}_{inj}$ represent the mass flow rates of the main and injected flows, respectively, while $\overline{P_{t1}}$, $\overline{P_{t2}}$, and $\overline{P_{t,inj}}$ denote mass flow averaged total pressures at the tandem stator inlet, outlet, and injection slot, respectively. This relationship takes into account the total pressure losses with respect to the total kinetic energy in the tandem stator domain. When $\dot{m}_{inj}$ is equal to zero, we obtain the standard definition of the total pressure loss coefficient (ω).

Taking Equation 5 into consideration, we present an example illustrating an injection strategy that accounts for injection losses. As before, the normalized axial location is set at $\zeta = 1.4$. However, this time a circumferential width w_c of 6 mm and an injection rate ratio $\dot{m}_{\text{inj}}/\dot{m}_{\text{stall}}$ of 0.25% are chosen to minimize the generated losses. This configuration results in a momentum coefficient C_u of 0.01 and a ratio u_{inj}/u_∞ of 1.2, in contrast to the enhanced configuration presented in Section 4.4, which had $C_u = 0.05$ and $u_{\text{inj}}/u_\infty = 2.1$.

As shown previously in Figure 14, the reduction of entropy along the axial direction after the injection location indicates effective mixing of the injected flow with the main flow. However, the entropy contours at the Stator casing, shown in Figure 22, reveal an increase in entropy due to the injection itself. This necessitates consideration of additional losses using Equation 5. For the larger momentum coefficient case ($C_u = 0.05$), the total pressure loss coefficient ω_t is 0.0494, which is slightly higher than in the smooth casing case. In contrast, for the smaller momentum coefficient case ($C_u = 0.01$), the calculated total pressure loss coefficient ω_t is 0.04396, compared to 0.04350 when injection effects are not considered, indicating that the injection-induced losses are negligible. Despite this, the calculated ω_t still represents a reduction of 5.1% compared to the smooth casing case, where ω is approximately 0.0462. Additionally, an increase in polytropic efficiency η_{tt} of about 0.28% is observed.

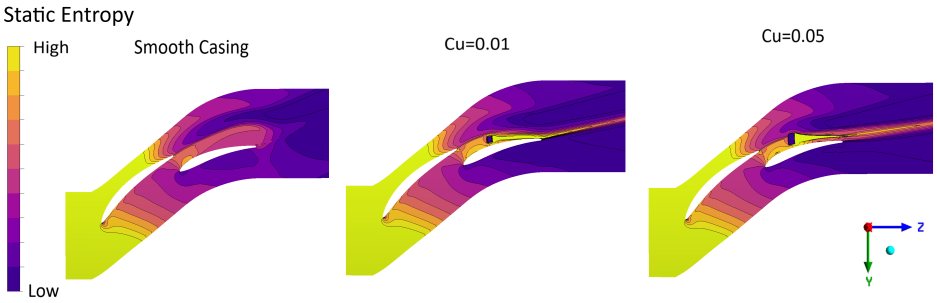

Figure 22: Comparison of the effects on static entropy at the Stator casing for the smooth casing case and different injection strategies: small ($C_u = 0.01$) and larger ($C_u = 0.05$) momentum coefficients.

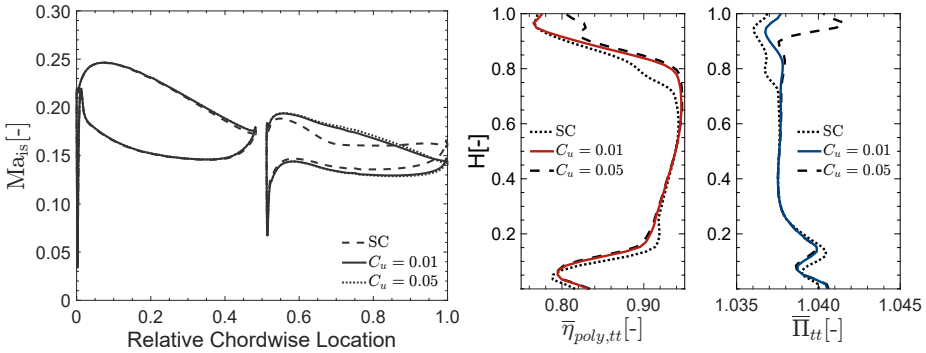

Figure 23: Comparison of injection strategies with small ($C_u = 0.01$) versus larger ($C_u = 0.05$) momentum coefficients to minimize injection losses, for cases at $\zeta = 1.4$. Left: Blade loading profiles at $H = 0.9$ showing $\mathrm{Ma_{is}}$; Right: Polytropic efficiency profile and total pressure ratio.

Figure 23 shows the comparison of this injection configuration ($C_u = 0.01$) with the smooth casing case and the equivalent higher momentum coefficient configuration ($C_u = 0.05$). A lower momentum coefficient configuration yields a lower increment but still offers aerodynamic improvements. As seen in the efficiency and pressure ratio profiles, the main difference is the behavior at span values $H > 0.9$, very close to the casing, where the higher momentum jet shows a pronounced influence. However, the effect of unlocking more diffusion in the rear vane of the tandem stator remains with smaller injection rates, as observed in the blade loading profiles. This approach presents a conservative method to account for injection losses. However, further adjustments may be necessary for each specific application. For instance, utilizing a recirculation channel to extract air from the endwall region of the second-stage rotor and re-inject it into the tandem stator in the first stage could enhance performance in other critical areas of the compressor, such as mitigating rotor tip leakage. This highlights the importance of an integrated approach to flow control evaluation, rather than relying on isolated assessments.

5 CONCLUSIONS

The implementation of air injection was numerically studied in a tandem stator shroud of a low-speed axial compressor, with the primary goal of enhancing compressor performance. The analysis of the smooth casing case identified flow separation issues in the stator flow, producing significant aerodynamic losses, leading to efficiency drops and suggesting the potential application of air injection to mitigate these effects. As a starting point, an injector baseline configuration was selected, and subsequently, a detailed parametric study was conducted to find the optimal locations and geometrical features of the injection slots. The parametric study indicated that each injection parameter significantly impacts aerodynamic performance: lowering the inclination angle (α) improves stage efficiency by facilitating smoother integration of injected air, optimizing the jet angle (β) is essential

for aerodynamic benefits, and an increased radius of curvature (R_c) is beneficial through an enhanced Coanda effect. Moreover, the relationship between circumferential width (w_c) and relative injection mass flow rate ($\dot{m}_{\text{inj}}/\dot{m}_{\text{stall}}$) emphasizes the need for a careful balance between injection velocity and momentum to achieve desired aerodynamic improvements without adversely affecting flow stability. The study further identified the direct relationship of the momentum coefficient (C_u) and velocity ratio (u_{inj}/u_∞) with improvements in efficiency and pressure ratios. The final Enhanced Configuration featured a circumferential width w_c of 10 mm and an injection mass flow rate ratio $\dot{m}_{\text{inj}}/\dot{m}_{\text{stall}}$ of 0.75%, demonstrating performance enhancements, achieving a 0.45% increase in polytropic efficiency (η_{tt}) and a 0.049% increase in pressure ratio (Π_{tt}) over the smooth casing scenario.

Optimal injector locations were identified within the transition area between the front and rear vanes, particularly on the suction side of the rear vane at ζ values of 1 to 1.4, reaching a maximum efficiency increment of 0.462% for $\zeta = 1.2$, just upstream of the separation point, confirming similar conclusions found in single aerofoil configurations. The example case with air injection at $\zeta = 1.2$ showed blade loading enhancement in the rear vane, evident from the increased diffusion factor and stator turning, effectively mitigating corner separation and improving flow dynamics at the design point. Under off-design conditions, the analysis demonstrated that injector locations near the rear vane optimize stage efficiency across a broad range of operating conditions, outperforming the smooth casing scenario, especially between normalized mass flow rates of 0.9 to 1.1. However, despite these efficiency improvements, the injection strategy does not extend the stall margin, predominantly due to limitations imposed by rotor tip flow characteristics.

While the scope of the study was to analyze the aerodynamic effects of air injection strategies in a tandem stator configuration, it is essential to acknowledge that implementing such strategies in real-world scenarios may introduce additional losses. Through a specific example incorporating total losses, our study demonstrated that a positive injection strategy remains viable, albeit with lower mass flow rates or momentum coefficients to keep additional losses to a minimum. This finding emphasizes the potential of air injection as a beneficial aerodynamic strategy in tandem stator configurations, provided that it is implemented with precision and a comprehensive understanding of its impact on overall system efficiency.

REFERENCES

[1] C.-T. DINH and K.-Y. KIM, "Effects of air injection on aerodynamic performance of a single-stage transonic axial compressor," in *conferences 2016 barcelona: EAB*, vol. 6, 2016.

[2] C.-T. Dinh, S.-B. Ma, and K.-Y. Kim, "Aerodynamic optimization of a single-stage axial compressor with stator shroud air injection," *AIAA journal*, vol. 55, no. 8, pp. 2739–2754, 2017.

[3] Z. Cao, X. Gao, X. Zhang, F. Zhang, and B. Liu, "Influence of endwall air injection with discrete holes on corner separation of a compressor cascade," *Journal of Thermal Science*, vol. 30, no. 5, pp. 1684–1704, 2021.

[4] Z. Cao, C. Song, X. Gao, X. Zhang, F. Zhang, and B. Liu, "Effects of pulsed endwall air injection on corner separation and vortical flow of a compressor cascade," *Engineering Applications of Computational Fluid Mechanics*, vol. 16, no. 1, pp. 879–903, 2022.

[5] J. Brent and D. Clemmons, "Single-stage experimental evaluation of tandem-airfoil rotor and stator blading for compressors, part 8," tech. rep., 1974.

[6] K. Bammert and H. Beelte, "Investigations of an axial flow compressor with tandem cascades," 1980.

[7] A. Tesch, M. Lange, K. Vogeler, J. Ortmanns, E. Johann, and V. Gümmer, "An experimental investigation of a tandem stator flow characteristic in a low speed axial research compressor," in *Turbo Expo: Power for Land, Sea, and Air*, vol. 45608, p. V02AT37A029, American Society of Mechanical Engineers, 2014.

[8] J. Foret, D. Franke, F. Klausmann, A. Schneider, H.-P. Schiffer, B. Becker, and H. Müller, "Experimental aerodynamic and aeroelastic investigation of a highly-loaded 1.5-stage transonic compressor with tandem stator," *International Journal of Turbomachinery, Propulsion and Power*, vol. 6, no. 3, p. 21, 2021.

[9] J. Eckel and V. Gümmer, "Numerical investigation of compressor tandem aerofoils featuring near-endwall modification," in *Journal of Physics: Conference Series*, vol. 1909, p. 012019, IOP Publishing, 2021.

[10] L. Zhang and S. Wang, "A combination application of tandem blade and endwall boundary layer suction in a highly loaded aspirated compressor outlet vane," *Proceedings of the Institution of Mechanical Engineers, Part A: Journal of Power and Energy*, vol. 232, no. 2, pp. 129–143, 2018.

[11] M. Straccia and V. Gümmer, "Numerical investigation of non-axisymmetric end wall contouring effects in a low-speed compressor tandem stator," in *14 th European Conference on Turbomachinery Fluid dynamics & Thermodynamics*, EUROPEAN TURBOMACHINERY SOCIETY, 2021.

[12] M. Hopfinger and V. Gümmer, "Preliminary design of a three-stage low-speed research compressor using tandem vanes," in *AIAA Propulsion and Energy 2019 Forum*, 2019.

[13] T. Panitz and D. Wasan, "Flow attachment to solid surfaces: the coanda effect," *AIChE Journal*, vol. 18, no. 1, pp. 51–57, 1972.

[14] A. J. Strazisar, M. M. Bright, S. Thorp, D. E. Culley, and K. L. Suder, "Compressor stall control through endwall recirculation," in *Turbo Expo: Power for Land, Sea, and Air*, vol. 41707, pp. 655–667, 2004.

[15] I. Ansys, *Ansys CFX, Release 24.2, Help System, CFX-Solver Theory Guide*. Ansys, Inc., 2024. Chapter 3.

[16] NUMECA International, *IGG/AutoGrid5 User's Guide*, (2013).

[17] I. Celik, U. Ghia, P. Roache, C. Freitas, H. Coleman, and P. Raad, "Journal of fluids engineering editorial policy statement on the control of numerical accuracy," 2000.

[18] L. Baojie, C. Zhang, A. Guangfeng, F. Du, and Y. Xianjun, "Using tandem blades to break loading limit of highly loaded axial compressors," *Chinese Journal of Aeronautics*, vol. 35, no. 4, pp. 165–175, 2022.

[19] H. Khaleghi, J. Teixeira, A. Tousi, and M. Boroomand, "Parametric study of injection angle effects on stability enhancement of transonic axial compressors," *Journal of Propulsion and Power*, vol. 24, no. 5, pp. 1100–1107, 2008.

[20] J. D. Denton, *Loss mechanisms in turbomachines*. 1993.

[21] S. W. Evans and H. P. Hodson, "The cost of flow control in a compressor," in *Turbo Expo: Power for Land, Sea, and Air*, vol. 54679, pp. 1–12, 2011.

[22] H. Kim, G. Rajesh, T. Setoguchi, and S. Matsuo, "Optimization study of a coanda ejector," *Journal of Thermal Science*, vol. 15, pp. 331–336, 2006.

[23] A. F. N. Sarimurat and A. F. N. Dang, "An analytical model for boundary layer control via steady blowing and its application to naca-65-410 cascade," *[Journal Name]*, vol. [Volume Number], no. [Issue Number], p. [Page Numbers], 2013.

[24] M. Hopfinger and V. Gümmer, "Numerical investigation of stator shroud leakage effects in a 1.5-stage low-speed axial compressor," in *14 th European Conference on Turbomachinery Fluid dynamics & Thermodynamics*, EUROPEAN TURBOMACHINERY SOCIETY, 2021.

[25] L. Fottner, "Theoretical and experimental investigations on aerodynamically highly-loaded compressor bladings with boundary layer control," in *4th International symposium on air breathing engines*, p. 7032, 1980.